OPEN ACCESS
IOP Publishing
Measurement Science and Technology
Meas. Sci. Technol. **35** (2024) 095407 (14pp)
https://doi.org/10.1088/1361-6501/ad5224

Non-invasive temperature monitoring in fixed-bed reactors by electrical capacitance tomography

Michael Weiss[1,2,*], **Alice Fischerauer**[1], **Andreas Jess**[2] and **Gerhard Fischerauer**[1]

[1] Chair of Measurement and Control Systems, Center of Energy Technology, University of Bayreuth, Bayreuth, Germany
[2] Chair of Chemical Engineering, Center of Energy Technology, University of Bayreuth, Bayreuth, Germany

E-mail: mrt@uni-bayreuth.de

Received 24 January 2024, revised 7 May 2024
Accepted for publication 30 May 2024
Published 12 June 2024

Abstract

Knowledge of the temperature distribution in fixed-bed reactors is of great importance for process control and optimization in many processes of the chemical industry. The state of the art is defined by invasive measuring methods for temperature measurement in such reactors. However, all invasive methods influence both the structure of the fixed-bed and the flow conditions and thus falsify the measurement results compared to real undisturbed conditions in a fixed-bed, above all with regard to the radial temperature profile. In addition, the temperature distribution in the entire reactor is usually derived from a few discrete measuring points based on a model, which sometimes results in large deviations from reality. In this article, electrical capacitance tomography (ECT) is explored as an alternative, non-invasive measurement method to monitor the temperature distribution inside fixed-bed reactors. The method exploits the temperature dependence of the effective bulk permittivity of the reactor filling. By way of an example, this dependence has been investigated in this work for two different hydrogenation catalysts. A temperature-resistant ECT sensor has been designed to perform measurements under the influence of temperature. The investigations show that, with the aid of ECT, it is possible to detect relative temperature changes in the region of interest with the materials examined.

Keywords: ECT, electrical capacitance tomography, fixed-bed reactor, temperature profile, non-invasive, temperature monitoring

* Author to whom any correspondence should be addressed.

List of symbols

Symbol	Unit	Description
C	F	Capacitance
$\boldsymbol{C}$	F	Vector of measured capacitances
ΔC	F	Change in capacitance
C_{Air}, C_{MUT}	F	Capacitance of empty and filled measuring cell
$C_{\mathrm{Air,\,ideal}}$,$C_{\mathrm{MUT,\,ideal}}$	F	Capacitance of empty and filled ideal capacitor
C_{FE}	F	Capacitance due to fringe effects
C_{min}, C_{max}	F	Smallest and largest capacitance in vector $\boldsymbol{C}$
f	Hz	Frequency
$\boldsymbol{g}$	—	Vector of normalized pixel permittivities
g_k	—	Permittivity in kth pixel
k	—	Index of current pixel
ℓ	m	Length of measuring cell
m	—	Number of measurement electrodes
M	—	Number of measured capacitances
N	—	Number of pixels
R	Ω	Resistance
r_{i}, r_{o}	m	Radius of inner electrode and inner radius of outer electrode of measuring cell
s	F^{-1}	Sensitivity coefficient
$\boldsymbol{S}$	—	Normalized sensitivity matrix
t	s	Time variable
U	V	Potential difference
$\underline{Z}$	Ω	Complex electrical impedance
$\lvert\underline{Z}\rvert$	Ω	Magnitude of complex impedance
$\arg\{\underline{Z}\}$	°	Phase of complex impedance
$\mathrm{Im}\{\underline{Z}\}$	Ω	Imaginary part of complex impedance
$\mathrm{Re}\{\underline{Z}\}$	Ω	Real part of complex impedance
ε_0	As/(Vm)	Electric field constant
$\Delta\varepsilon$	—	Change in relative permittivity
$\varepsilon_{r,\,\mathrm{eff}}$	—	Effective relative permittivity
$\varepsilon_{r,\,\mathrm{eff}}(\vartheta)$	—	Permittivity-temperature relationship
$\varepsilon_{r,\,\mathrm{low}}$, $\varepsilon_{r,\,\mathrm{high}}$	—	Relative permittivity for low and high calibration of ECT system
$\varepsilon_{r,\,\mathrm{norm}}(\vartheta)$	—	Normalized permittivity-temperature relationship
$\varepsilon_{r,\,\mathrm{MUT}}$	—	Relative permittivity of the material under test (MUT)
$\varepsilon(x,y)$	—	Permittivity distribution
Γ	m^2	Electrode surface
ϑ	°C	Temperature variable
ϑ_k	°C	Temperature in kth pixel
ϑ_{min}, ϑ_{max}	°C	Temperature at low and high calibration of ECT system
$\vartheta_{\mathrm{start}}$	°C	Temperature start value for Newton-Raphson method
$\vartheta(x,y)$	°C	Temperature distribution
$\boldsymbol{\lambda}$	—	Vector of normalized capacitances
ρ	m	Radial coordinate
$\phi(x,y)$	V	Potential distribution
ω	s^{-1}	Angular frequency

1. Introduction

Many large-scale, heterogeneously catalyzed exo- or endothermic gas-phase reactions are carried out in wall-cooled or -heated fixed-bed reactors, respectively. To avoid critical operating conditions (in case of exothermic reactions) and to maximize product yields, fixed-bed temperature measurements (and control) is required for the reliable and safe operation of such reactors. However, this requires the exact knowledge of the local (radial) heat transfer within the fixed-bed to the reactor wall and from the wall to the heat transfer medium used for cooling or heating, e.g. boiling water, mineral oils, or molten salts. Therefore, the axial and radial temperature distribution in fixed-bed reactors has been the subject of numerous research efforts in recent decades.

In most publications, the heat transport phenomena in fixed-bed reactors are described by means of established approaches and models. These models usually simplify the heat transfer by certain assumptions, for example by homogenizing the solid and gas phases by a so-called pseudo-homogeneous fixed-bed and/or by utilizing effective radial heat transport parameters such as a constant effective thermal conductivity in the bed, an internal heat transfer coefficient at the internal wall, and an external heat transfer coefficient to consider the heat transfer from the external reactor wall to the cooling/heating medium. The predictions of these models can show large deviations from reality, especially for reactions with a large reaction enthalpy. Therefore, a better experimental validation is required with regard to a more reliable basis for reactor design and control.

Many tests have already been carried out to measure radial and axial heat transfer and the corrsponding temperature profiles. Most of the measurement setups involve the installation of fixed thermocouples at defined radial and axial positions in the fixed-bed reactor. Instead or in addition to this, thermocouple guide tubes are also inserted into the fixed-bed mostly in axial but also in radial direction, along with temperature measurements carried out at arbitrary points using movable thermocouples [1–3]. Such invasive methods lead to a falsification of the measurement results compared to a 'real' undisturbed fixed-bed due to a strong manipulation of the bed properties (e.g. of the radial fluid velocity profile) and heat dissipation via the guide tubes as well as the thermocouples themselves. In addition, measurements are often taken only at discrete points and the entire temperature distribution is roughly interpolated based on these measurements, so that local hotspots are possibly disregarded.

The ideal solution to these problems is the non-invasive measurement of the entire radial and axial temperature distribution within fixed-bed reactors. With this in mind, it is of interest to develop and establish alternative measurement methods that allow heat transfer phenomena in fixed-bed reactors to be recorded and described realistically. To the authors' best knowledge, only experiments with fiber-optic

measurement techniques [4] as well as nuclear magnetic resonance methods [5] have been carried out so far.

With the former technology, temperatures can be measured with treated glass fibers at various points along a fiber via the reflection behavior of the injected light. The influence on the structure of the fixed-bed is reduced by the smaller fiber diameter of at least 130 µm compared to larger thermocouples or thermocouple guide tubes, typically with a diameter of some mm [6]. However, the measurement method still requires the installation of external objects in the packed bed and is therefore still invasive. In addition, to acquire the axial and radial temperature profiles of a reactor, multiple fibers must be placed in the fixed-bed, which continues to affect the porosity and velocity profiles in the bed. As before, the determination of the overall temperature distribution is then still strongly model-based.

Using nuclear magnetic resonance (NMR), ethylene glycol-filled glass capsules are integrated into the fixed-bed. This allows temperature measurements via the temperature dependence of the fluid for temperatures of up to 140 °C [5]. The disadvantage of this is again the introduction of other materials into the fixed bed, which usually differ greatly in their geometry, size and material properties from the rest of the bed. In addition, the temperatures in the hot reaction zone of many technically relevant chemical reactions are far above the specified maximum temperature of this method ($<$140 °C) for strongly exothermic reactions, which strongly limits the application range of the method in industrial chemistry. In addition, NMR-based methods are expensive.

A non-invasive measurement method that could be used to measure the temperature distribution in fixed-bed reactors without affecting the packed bed structure is electrical capacitance tomography (ECT). Here, a large number of measuring electrodes are mounted on the surface of a detection region, for example a tube, and the capacitances of all possible electrode combinations are measured. The permittivity distribution within the detection region is then reconstructed from the measured capacitances using inverse computation algorithms.

So far, ECT has been used for a wide range of applications. The main field of application is still process monitoring, for example in the investigation of multiphase mixtures in pipelines [7]. In chemical reaction engineering, the method has already been used in particular to identify flow regimes in fluidized bed reactors [8]. Other applications are fill-level monitoring in weightless environments [9], the identification of flame characteristics [10], or the monitoring of the casting process of metal foundry parts [11].

In order to make ECT suitable for high-temperature applications, the development of temperature-resistant electrode arrangements is a crucial aspect. While conventional and inexpensive materials can be used in most applications, high demands are placed on insulation materials, gaskets, sealants and adhesives as well as cables and electrical contacts at temperatures around and above 200 °C. In addition, the use of various materials also results in different coefficients of thermal expansion, which leads to mechanical stress in addition to thermal stress. To date, high-temperature ECT sensors have been developed in the literature that use either glass [8, 12] as insulators or ceramics in conjunction with sintered electrodes [13–15] for maximum temperature resistance. In this article, a simplified demonstrator for temperatures up to 250 °C is described and discussed in section 4.1.

The application of ECT for locally resolved temperature measurement is still mostly unexplored. In order to use the measurement technique for this purpose, the electrical material properties of the materials under investigation need to exhibit a sufficiently large temperature dependence (what exactly 'sufficient' is to mean in the given context also needs to be explored and is still not clear). If for example the temperature-permittivity relationship of a material is known, the temperature distribution in the material can be estimated from the reconstructed permittivity distribution. With this in mind, experiments have already been carried out to investigate the extrusion temperature in polymer injection molding machines and to monitor the cooling process of plastic pellets after production [16, 17]. Another study focused on estimating the temperature field of a flame from combined conductivity and permittivity measurements [12]. The experiments have shown that it is in principle possible to measure temperatures spatially resolved with the help of ECT, which makes the measurement method also interesting for the application in reaction engineering. However, the authors are not aware of any publications to date that have investigated the applicability of ECT for temperature measurement in fixed-bed reactors.

The aim of this paper is to show to what extent ECT is suitable for monitoring the temperature of fixed-bed reactors. For this purpose, the temperature dependence of the permittivity of various bulk materials has first been investigated by means of impedance measurements. Then an ECT measurement setup has been developed and used to carry out experiments at various temperatures using ECT with the same bulk solids.

2. Electrical capacitance tomography

An ECT system includes a detection region with an array of electrodes at the region surface, often called 'sensor', a measuring device for switching between the different pairs of electrodes and for recording the associated capacitances, and a PC for controlling the measurement, data storage, data processing, and image reconstruction (figure 1). The detection region can have arbitrary shape, but in process engineering circular tubes are of most interest as circular symmetry promises homogeneous flow and reaction conditions. The electrode arrangement consists of one or more rings of usually 6–16 measuring electrodes, each of which is distributed equidistantly around the detection volume.

To measure the partial capacitances, an AC voltage is applied to one pair of electrodes, while all other electrodes are grounded. The capacitance between the electrodes is determined from the resulting electrical current. Following this, a switch connects the next electrode pair with the capacitance measurement unit. This procedure is repeated until all electrode combinations have been measured. For example, a

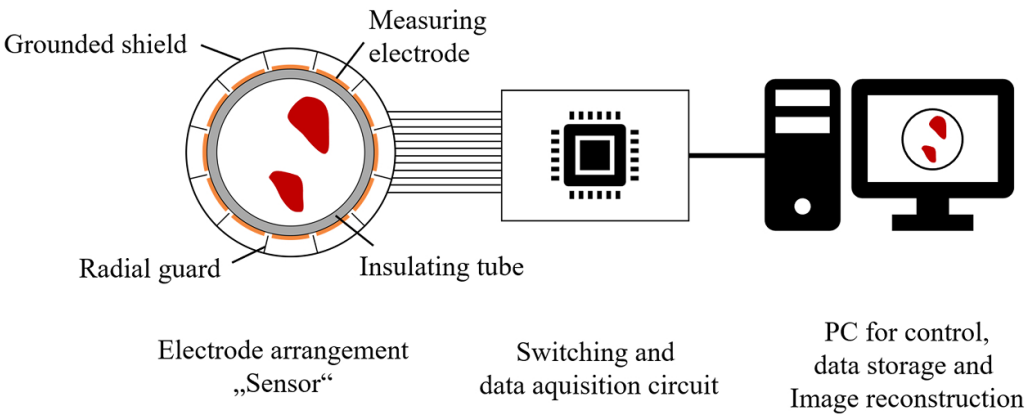

Figure 1. Setup of an ECT-measurement system.

number of electrodes of $m = 12$ electrodes results in $M = m \cdot (m-1)/2 = 66$ independent capacitance measurements. In order to reconstruct the permittivity distribution in the detection region on the basis of the capacitances, the region is divided into N discrete pixels (2-dimensional case) or voxels (3D case) within which the permittivity is assumed to be constant. In our experiments, we dealt with 2D reconstruction cases, which is why we will only speak of pixels in the remainder of this article.

The starting point for the image reconstruction is the relationship between capacitance and permittivity, which is usually nonlinear in real systems. For simple arrangements such as the parallel plate or the cylindrical capacitor, this relationship is linear. In ECT, however, more complex arrangements are used, which means that the capacitance between two conductors also depends on the permittivity distribution between them. The capacitance then results from:

$$C = -\frac{1}{U} \iint_{\Gamma} \varepsilon(x,y)\, \nabla\phi(x,y)\, \mathrm{d}\Gamma, \tag{1}$$

with the capacitance C the potential difference U between the electrodes, the permittivity distribution $\varepsilon(x,y)$, the potential distribution $\phi(x,y)$ and the electrode surface Γ [18].

In ECT applications, equation (1) is often linearized under the assumption of only small perturbations of the local permittivity $\Delta\varepsilon$ by neglecting higher order terms. In this approximation, the change of the capacitance ΔC as a function of a change of the permittivity in a pixel $\Delta\varepsilon$ can be written as

$$\Delta C = s \cdot \Delta\varepsilon. \tag{2}$$

Then, the proportionality factor s is constant and stands for the sensitivity connecting the small change in permittivity to a small change in capacitance. The discretization of the area of interest between the measuring electrodes and the use of normalized quantities leads to the following linear system of equations:

$$\underset{M\mathrm{x}1}{\boldsymbol{\lambda}} = \underset{M\mathrm{x}N}{\boldsymbol{S}} \cdot \underset{N\mathrm{x}1}{\boldsymbol{g}} \tag{3}$$

where $\boldsymbol{\lambda}$ is the vector of normalized capacitances, $\boldsymbol{g}$ is the vector of normalized permittivities in all of the pixels, and $\boldsymbol{S}$ is the sensitivity matrix. The latter contains the sensitivities of the capacitances of the individual electrode combinations to the permittivity changes of the individual pixels.

The calculation of the normalized capacitances based on known pixel permittivities is called the forward problem. When the capacitance values are available from a measurement and the pixel permittivities are the desired quantities, the inverse problem must be solved. This is an ill-posed problem, and the system of equations to be solved is usually severely underdetermined. For the latter reason, the sensitivity matrix $\boldsymbol{S}$ is not square and thus not invertible. As a result, the inverse problem does not have a unique solution and special approaches are needed to obtain qualitatively satisfactory results. With this in mind, a variety of reconstruction algorithms have been developed and improved over time, which can be divided into direct and iterative, as well as linear and nonlinear methods. In the context of the experiments presented here, a method based on the linear back projection algorithm (LBP) including sensitivity weighted filtering in a modified way is used [19, 20]. It essentially looks for a minimum-norm solution based on the pseudoinverse (Moore–Penrose inverse) of $\boldsymbol{S}$ [21].

By calculating the locally resolved permittivity distribution in a detection volume, ECT could provide a non-invasive measurement method for determining the temperature distribution in fixed-bed reactors. The basic requirement is a sufficient temperature dependence of the relative permittivity of relevant bulk materials used in the operation of such reactors.

In this study, the temperature dependence of the relative permittivity is determined using impedance measurements. How ECT and material characterization are combined to determine the spatially resolved temperature distribution is shown schematically in figure 2. In the following sections, the tests and evaluation of the material characterization are presented first, followed by the discussion of the ECT setup and the temperature experiments conducted.

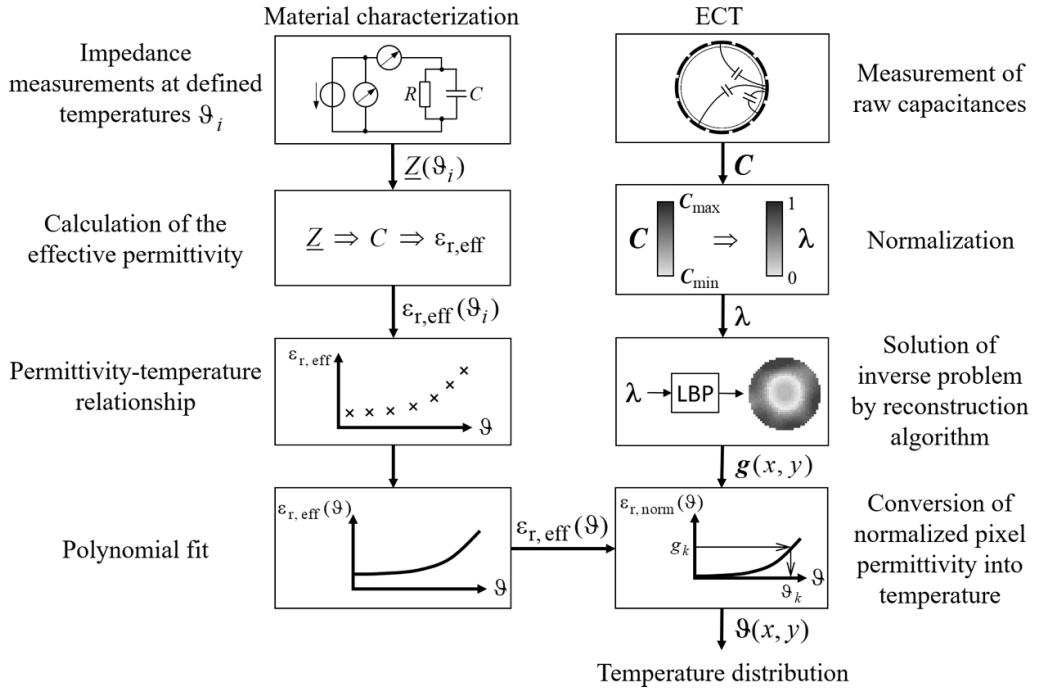

Figure 2. Overview of how the temperature distribution is derived from experimentally determined permittivity-vs.-temperature relationships in conjunction with permittivity distributions measured by ECT.

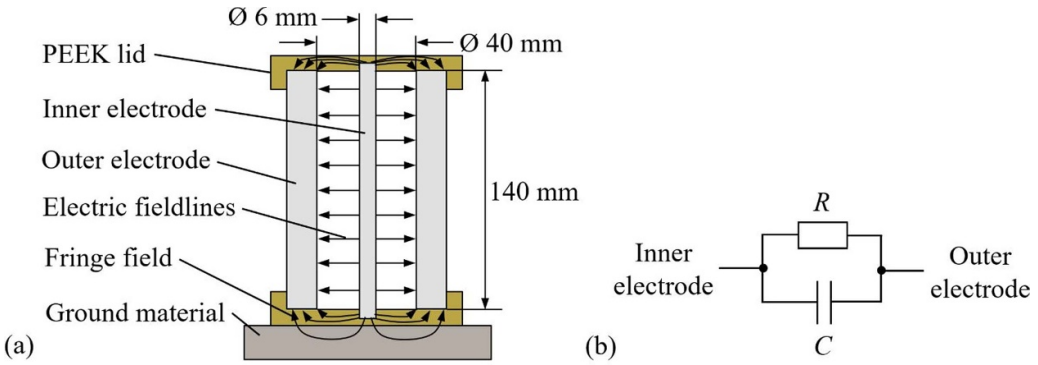

Figure 3. Impedance measuring cell: (a) Schematic representation (similar to [22]). (b) Equivalent circuit considering capacitive and resistive effects between the center electrode and the outer electrode.

3. Investigation of the temperature dependence of technically relevant materials by electrical impedance measurements

In order to investigate the temperature dependence of the electrical properties—permittivity and conductivity—of materials, impedance measurements are performed in this work. This involves experiments with glass spheres, which are often used in fixed-bed reactors as an inert material for diluting the catalyst or as a mixing section, as well as with two different nickel hydrogenation catalysts in fully oxidized form.

3.1. Measurement setup

For the measurements, a cylindrical measuring cell with radial dimensions similar to those of a cooled multi-tubular fixed-bed reactor (frequently used in industrial practise for highly exothermic reactions such as methanation, Fischer–Tropsch– or methanol synthesis) with an axial thermocouple guide tube was used. This ensured a bulk density distribution inside the measuring cell and therefore a measured impedance comparable to the values in actual applications. The outer electrode had an inner diameter of 40 mm, a wall thickness of 10 mm and a length of 140 mm (figure 3(a), based on [22]). The inner electrode had a diameter of 6 mm with a length of 150 mm and extended 5 mm into the upper and lower cover of the measuring cell for alignment. Aluminum was used for the electrodes, whereas the lids were made of polyether ether ketone (PEEK).

The sample-loaded measuring cell was placed in an electrically heated oven for the measurements and connected to the impedance measuring instrument (Keysight E4990A [23]) via coaxial cables. The measurement was controlled via an off-the-shelf desktop PC with LabVIEW software [24].

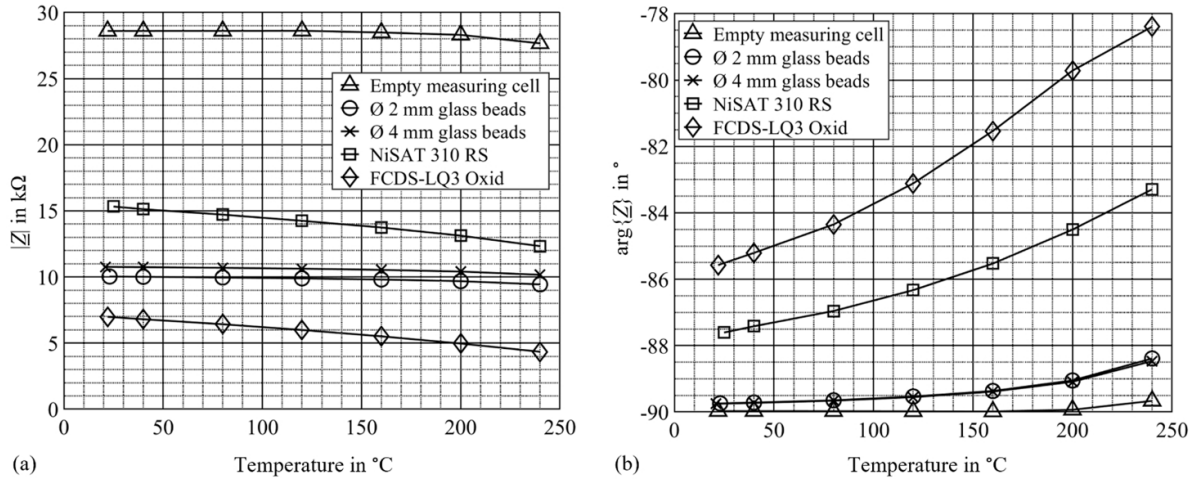

Figure 4. Measured electrical impedance $\underline{Z}$ of the measuring cell as a function of temperature for different materials at a frequency of 1 MHz. (a) Impedance magnitude $|\underline{Z}|$. (b) Impedance phase $\arg\{\underline{Z}\}$.

The measuring cell was heated up in steps of 40 °C starting at room temperature and going up to 240 °C. The actual furnace temperature was measured via a thermocouple inside the furnace and via the internal temperature sensor of the furnace itself. Ten campaigns of 200 repeated measurements each were carried out at each temperature level. Measurements were taken at a constant frequency of 1 MHz since this is the frequency of the ECT measurement system which was to be used later. During a measurement campaign, the heating current of the furnace was switched off to minimize interference. Between the campaigns, the heating was switched on again for at least 2 min to compensate for the temperature loss during the repeated measurements. Over the ten measurement campaigns, this resulted in a maximal temperature drop of approximately 2.5 °C at the maximum temperature of 240 °C.

3.2. Results and discussion

3.2.1. Measured impedances of empty and sample-loaded measuring cells. Figure 4 shows the measured impedance magnitude and phase for the empty and the sample-loaded measuring cell as a function of temperature. Modeling the empty cell as an ideal cylindrical capacitor with capacitance $C_{\text{Air, ideal}}$, one would expect the following electrical impedance at 1 MHz:

$$\underline{Z}_{\text{Air, ideal}} = \frac{1}{j\omega C_{\text{Air, ideal}}} = -\frac{j}{2\pi f}\cdot\frac{\ln(r_\text{i}/r_\text{o})}{2\pi\varepsilon_0\ell} \approx -\frac{j}{2\pi\cdot 1\,\text{MHz}}\cdot\frac{\ln(20\,\text{mm}/(3\,\text{mm}))}{2\pi\varepsilon_0\cdot 140\,\text{mm}} \approx -j38.8\,\text{k}\Omega, \tag{4}$$

with the imaginary unit j, the angular frequency ω, the frequency f, the electric field constant ε_0, the radii of the inner electrode r_i and outer electrode r_o and the length of the capacitor ℓ.

This does not depend on temperature except for the small thermal expansion effect of the capacitor length. By figure 4, the measured impedance was constant up to a temperature of about 150 °C and deviated from there more and more with increasing temperature. The low-temperature difference between measured and calculated impedance is attributed to fringing fields, which are neglected in the ideal-capacitor model, and the influence of the two PEEK lids, which are required to hold the inner electrode in place but are not included in the ideal-capacitor model. Both contributions increase the empty-cell capacitance over the value obtained by the idealized model, which corresponds to a decrease in the measured electrical impedance magnitude. Additionally, the material PEEK as well as filled in materials have a finite conductivity, which can be modeled by a shunt resistor as in figure 3(b).

The temperature-dependent change of the magnitude and phase values is explained by changes in the permittivity or conductivity of the PEEK lids on the one hand and by the thermal linear expansion of the aluminum electrodes on the other hand. The relative permittivity of PEEK increases with temperature, which also leads to an increase of the measuring cell capacitance and thus to a decrease of the impedance magnitude. The thermal expansion coefficient of aluminum is 24 ppm °C^{-1}. Hence, at a temperature of 200 °C, the capacitor electrodes are longer by about 0.5% compared to room temperature. Correspondingly, the capacitance increases by 0.5% and the apparent impedance decreases by 0.5%.

The temperature-dependent increase in the phase angle can be explained on the basis of the parallel model by an increase in conductivity and thus a decrease in the shunt resistance R with temperature.

For the characterization of bulk materials, the measuring cell was filled with the materials to be investigated. First, solid glass spheres made of soda-lime glass with a particle diameter of 2 mm were used. Figure 4 shows that the measured impedance magnitude is significantly lower compared to the empty measurement. In addition, a drop in the magnitude can also be observed, the absolute change of which is comparable to the empty measurement. The phase angle

Table 1. Characteristic particle and bulk properties of the materials examined.

Material	2 mm glass beads	4 mm glass beads	NiSAT 310 RS	FCDS-LQ3
Particle density in kg m^{-3}	2800	2650	1250	3150
Bulk density in kg m^{-3}	1600	1530	740	1900
Bed porosity	0.43	0.42	0.41	0.40
Mean particle length in mm	—	—	5.2	2.9
Mean particle diameter in mm	2.0	3.9	1.3	2.9
Equivalent spherical diameter in mm	2.0	3.9	2.4	3.3
Ni-content in wt%	—	—	56.7 [25]	63.6

appreciably deviates from −90° and changes with temperature even at lower temperatures.

Measurements with glass spheres 4 mm in diameter showed an almost identical temperature behavior of the impedance phase. The magnitude of the impedance, however, deviated noticeably, see figure 4(a). This is explained on the one hand by the finite measurement volume. For larger particles, the region of higher porosity (smaller packing density) near the cell wall is larger than for smaller particles. This leads to a higher relative air content in the measuring cell and thus a higher cell impedance. On the other hand, the number of particle contacts or current paths is larger for smaller particles, which is why an increasing impedance can also be expected with increasing particle diameter.

In addition to measurements with glass spheres, the commercially available nickel hydrogenation catalyst NiSAT 310 RS (56.7 wt% of nickel on an Al_2SiO_5/Al_2O_3 support [25]) from the company Clariant and the catalyst FCDS-LQ3 Oxid (63.6 wt% of nickel, composition of the support material not exactly known) from the former company Sued-Chemie have been investigated in oxidized form. To oxidize the catalysts, they were heated to 200 °C for several hours and repeatedly exposed to a stream of compressed air. Further properties of the investigated materials are listed in table 1.

Figure 4 shows that the impedance magnitude with the NiSAT catalyst is significantly higher compared to glass spheres, which is attributed to different material properties such as composition and shape. Moreover, the phase of the impedance starts at an angle of −87.6° at a furnace temperature of 25 °C and ends at a temperature of 240 °C with a value of approximately −83.15°. It is noticeable that the slope of the curves for the NiSAT catalyst are significantly steeper than in the case of glass spheres. This illustrates that the electrical material properties of the oxidized catalyst exhibit a stronger temperature dependence compared to the spherical glass particles.

The FCDS-LQ3 exhibits an even stronger temperature dependence. Its impedance magnitude lies significantly below the values of the other materials, while the slope of the curve is similar to that of the NiSAT catalyst. The corresponding phase angle also has the smallest absolute values over the entire temperature range with the steepest slope of all curves.

3.2.2. Calculation of an effective bulk permittivity. In order to be able to derive the temperature distribution from the permittivity distribution reconstructed by means of ECT, the temperature dependence of the relative permittivity of the substances used must be known. Against this background, an effective bulk permittivity can be calculated for each temperature investigated on the basis of the impedance data considered for glass spheres and the oxidized catalysts.

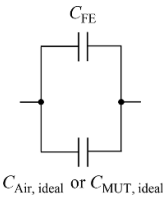

Figure 5. Equivalent circuit of the measuring-cell capacitance. C_{FE} denotes the fringe-effect capacitance and $C_{Air,\,ideal}$ and $C_{MUT,\,ideal}$ are the capacitances of the empty and the sample-filled ideal capacitor, respectively.

For this purpose, first the capacitive part of the measured impedance, modeled as shown in figure 3(b), is calculated. This is done by using the expressions for the real and imaginary parts of the complex impedance:

$$\mathrm{Re}\{\underline{Z}\} = \frac{R}{1+(\omega RC)^2}, \tag{5}$$

$$\mathrm{Im}\{\underline{Z}\} = -\frac{\omega R^2 C}{1+(\omega RC)^2}. \tag{6}$$

Since the angular frequency in the impedance measurement is known to be $\omega = 2\pi \cdot 1$ MHz and the real and imaginary parts can be determined from the measured magnitude and phase of the impedance, this system of equations can be solved for the capacitance C:

$$C = -\frac{\mathrm{Im}\{\underline{Z}\}}{\omega \cdot \left(\mathrm{Re}^2\{\underline{Z}\} + \mathrm{Im}^2\{\underline{Z}\}\right)}. \tag{7}$$

The capacitance C is composed of a capacitance C_{FE} due to fringe effects and an ideal capacitance $C_{Air,\,ideal}$ or $C_{MUT,\,ideal}$ due to the empty or sample-filled capacitor, respectively (figure 5; MUT = material under test).

For an ideal cylindrical capacitor (neglecting the fringe-effect) and under the assumption of homogeneous filling with the MUT the relative permittivity of the MUT $\varepsilon_{r,\,MUT}$ can be calculated through the ratio of the filled-cell capacitance $C_{MUT,\,ideal}$ to the empty-cell capacitance $C_{Air,\,ideal}$:

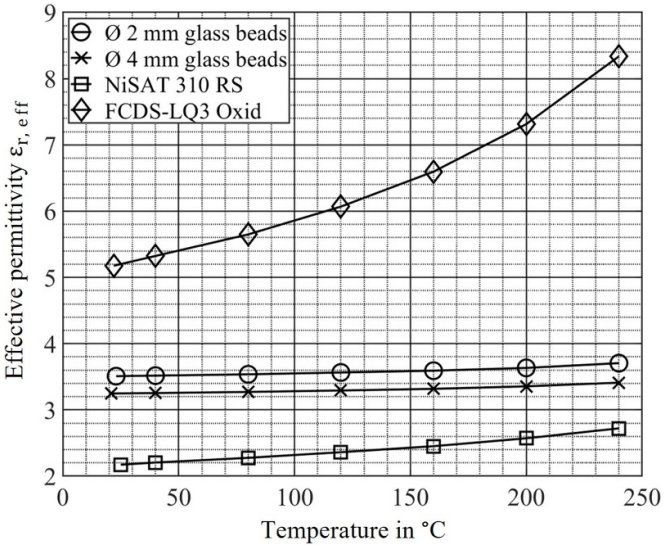

Figure 6. Effective permittivities calculated from measured impedances for various materials, plotted versus temperature (based on [22]).

$$\varepsilon_{r,\,\mathrm{MUT}} = \frac{C_{\mathrm{MUT,\,ideal}}}{C_{\mathrm{Air,\,ideal}}}. \tag{8}$$

Here,

$$C_{\mathrm{Air,\,ideal}} \approx \frac{2\pi\,\varepsilon_0 \cdot 140\ \mathrm{mm}}{\ln(2\ \mathrm{mm}/\,(3\ \mathrm{mm}))} \approx 4.1\ \mathrm{pF}. \tag{9}$$

The fringe-effect capacitance C_{FE} is calculated using $C_{\mathrm{Air,\,ideal}}$ and the empty-cell capacitance C_{Air} determined by equation (7) from the measured empty-cell impedance:

$$C_{\mathrm{FE}} \approx C_{\mathrm{Air}} - C_{\mathrm{Air,\,ideal}}. \tag{10}$$

With the use of this quantity, an effective bulk permittivity can then be calculated according to equation (8), which is at least partially corrected for the deviations occurring due to the fringe effect:

$$\varepsilon_{r,\,\mathrm{eff}} = \frac{C_{\mathrm{MUT}} - C_{\mathrm{FE}}}{C_{\mathrm{Air}} - C_{\mathrm{FE}}}, \tag{11}$$

with the sample-filled measuring cell capacitance C_{MUT} determined by equation (7) from the measured filled-cell impedance.

Applying equation (11) to the data presented in figure 4 leads to the permittivity-temperature relationships shown in figure 6. According to this, the effective permittivity of glass-sphere fillings ranges approximately between 3.25 and 3.7 whereas the effective permittivity of the NiSAT catalyst is significantly below this range of values. The curves for the 2 mm and the 4 mm glass spheres run almost parallel to each other which illustrates the similar temperature dependency. The offset between the two curves could be explained by the higher number of particle contacts and therefore current paths in case of the smaller beads. In contrast, the temperature dependence of the material properties of the NiSAT catalyst is slightly more distinct than in the case of the glass beads. By comparison, the effective permittivity of the filling with the FCDS-LQ3 catalyst has the largest values and the strongest temperature dependence by far. In any case, the curves shown in figure 6 allow one to estimate temperature distributions from ECT-measured permittivity distributions. The error will be the smaller, the steeper the $\varepsilon_{r,\,\mathrm{eff}}(\vartheta)$ curve is.

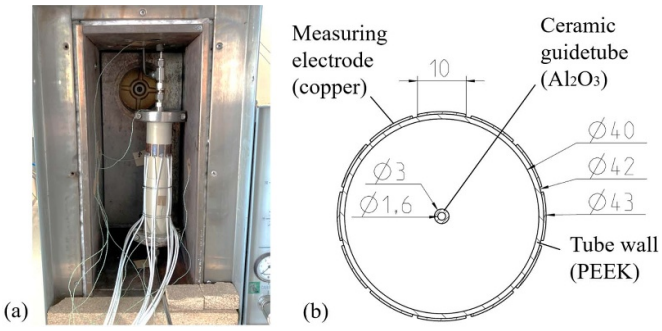

Figure 7. Measurement setup. (a) Photograph of the PEEK tube with measuring electrodes and thermocouples inside the furnace chamber. (b) Cross-sectional view at the height of the electrode ring.

4. Experiments to investigate the suitability of ECT for temperature monitoring in fixed bed reactors

4.1. ECT measurement setup

To investigate the suitability of ECT for monitoring the temperature of fixed-bed reactors, a demonstrator setup made of a circular PEEK tube with a single electrode ring with 12 electrodes has been realized. The setup allows measurements at temperatures of up to 200 °C. It consists of a PEEK tube with an inner diameter of 40 mm and a wall thickness of 1 mm. The tube is sealed on both sides by an ISO-KF flange with a transition to a compression fitting, see figure 7(a). The limiting component in terms of temperature (200 °C) are the o-ring seals sitting in the flange, which can be replaced with a more temperature-resistant version if necessary. The measuring electrodes are glued to the PEEK tube with a temperature-resistant silicone sealing compound. The copper electrodes are adapted to the curvature of the PEEK tube and have an area of about 20 mm × 10 mm as well as a thickness of 0.5 mm. The shielded signal cables are temperature-resistant up to 250 °C and are soldered to the electrodes using a solder with a melting point higher than 300 °C.

The commercially available ECT system m3c from the manufacturer Industrial Tomography Systems [26] was used to record the capacitances and reconstruct the tomograms shown. The algorithm used is based on LBP with the integration of sensitivity weighted filtering as shown in [19] as well as modifications to this method as presented in [20].

During the measurements, the tube was placed in a convection oven, which was used to heat up the whole structure. The aim of the experiments was to generate radial and axial temperature gradients and to detect them with ECT for the materials presented in section 3. To generate the temperature gradients, cold gas was injected into the tube to cool down the heated

Figure 8. Photograph of the complete measurement setup with furnace, short gas supply line through furnace ceiling, mass flow controllers, and compressed air supply.

fixed-bed. This was done via a short gas supply line which runs through the furnace ceiling, see figure 8. For comparison's sake, a ceramic thermocouple guide tube was installed along the axis of the tube.

4.2. Experimental procedure

For the temperature tests, the demonstrator was operated either empty or with a catalyst filling. It was placed inside the furnace and connected to the gas tubing. At room temperature, the ECT measuring device was calibrated to the minimum reference permittivity in each case. The furnace was then switched on and heated up to approximately 200 °C. After heating up the furnace, this temperature was maintained for at least two hours to allow the demonstrator and its contents to heat up. The instantaneous furnace temperature was measured via several thermocouples installed inside the heating chamber. The fixed-bed core temperature was also recorded during heating up via the installed guide tube. After completion of the heating process, the ECT system was calibrated to the maximum reference permittivity. The absolute numerical values for the lower and upper reference permittivities were selected on the basis of the respective temperature-permittivity relationship from figure 6.

After the calibration, a defined air stream of 620 l h^{-1} was passed through the bed via a mass-flow-controller while the furnace continued to maintain a constant ambient temperature outside the tube. The gas flow was applied for two hours until a steady-state temperature distribution was established. The gas flow was then shut off and the bed was reheated for another two hours to identify drift phenomena or systematic errors. The furnace was then switched off and the cooling process was monitored via the ECT system in like manner.

4.3. Results and discussion

4.3.1. Tomograms of measurements with empty and filled demonstrator. Temperature tests were carried out with an empty tube in order to investigate the temperature influence of the tube wall material. For calibration, reference permittivities of $\varepsilon_{r,\,\mathrm{low}} = 1$ for room temperature and an arbitrary value of $\varepsilon_{r,\,\mathrm{high}} = 2$ for 200 °C were used in the calibration procedure of the ECT measurement system. For the measurements with filled tube the respective values from figure 6 at room temperature and 200 °C were used. Figure 9(a) shows the tomograms obtained. From time t = 0, a cold air flow ($\vartheta = 20$ °C) was directed through the tube in order to cool the tube wall and in the filled case also the fixed bed from the inside. All shown tomograms were filtered to a rate of one frame per second and averaged over time with a moving time window over 20 frames before plotting.

In the case of the empty tube a low-permittivity (i.e. low-temperature) region forms in the immediate proximity of the wall after only a few seconds. This is consistent with experiments by Ho and Jow [27] who have shown that the relative permittivity of PEEK increases with temperature. The injected air stream cools the tube wall and thus leads to a smaller wall permittivity. Of course, it also cools the tube interior, but the permittivity of air does not depend strongly on temperature, which is why this temperature effect cannot be 'seen' by the ECT system. If one compares the time scales for the empty and the filled measurements, it becomes clear that the low permittivity region near the wall forms faster in the empty measurement since there is no bulk material delaying the cooling process of the wall due to its heat capacity.

When the experiment is repeated with Ø2 mm glass spheres, the effective bulk permittivity of which changes only slightly with temperature according to figure 6, the reconstructed tomograms show that the wall influence observed in the empty measurement dominates. An expected drop of the normalized permittivity in the center of the fixed-bed due to the falling temperature cannot be detected.

If the measurement is carried out with the oxidized NiSAT catalyst, the effective bulk permittivity of which already exhibits a stronger temperature dependence, the wall effect still appears to have a significant influence on the reconstructed permittivity distribution. However, it can be seen here that the temperature dependence of the fill also plays a non-negligible role. The normalized permittivity also decreases with time at the core but fluctuates over time, which becomes particularly clear when comparing the tomograms at $t = 15$ min, $t = 20$ min and $t = 25$ min. It is assumed that the temperature-dependent difference in permittivity is still too small in comparison to disturbing influences and the resolution of the measuring device.

This assumption is supported by looking at the tomograms of the measurement with the FCDS-LQ3 catalyst, which showed by far the greatest temperature dependence in the material characterization. With the addition of the compressed air flow, the lowest normalized permittivity is observed in the middle of the tube and the highest near the tube wall. The influence of the wall seems to play only a subordinate role here compared to the fill. As this catalyst was the only one of the materials investigated to exhibit sufficient temperature dependence for ECT, it will be examined in more detail in the following sections.

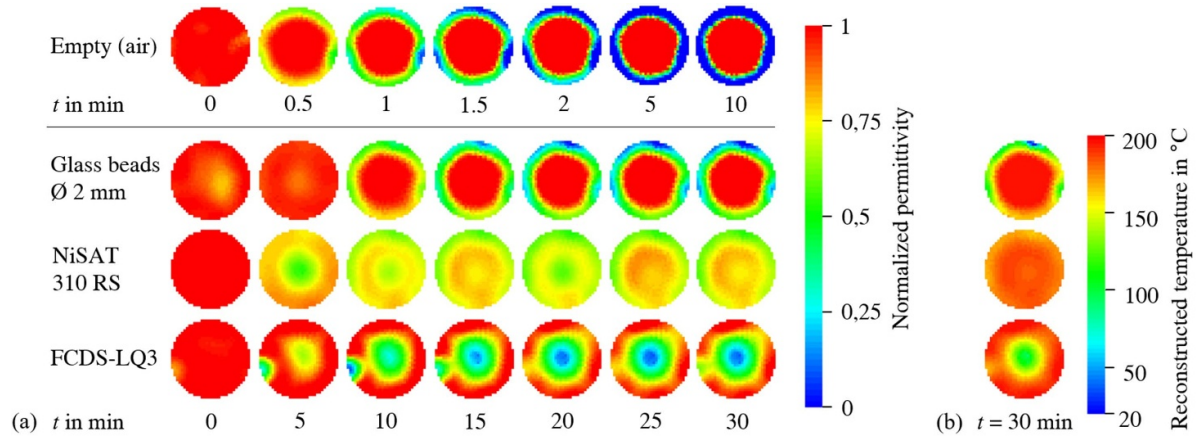

Figure 9. Reconstruction results for an ECT measurement with empty (i.e. air-filled) demonstrator tube as well as fillings with Ø2 mm glass beads, the NiSAT RS 310 catalyst, and the FCDS-LQ3 catalyst. Injection of a compressed air flow from time $t = 0$. Pixel permittivities and temperatures smoothed by time-averaging (moving time window over 20 frames at a rate of one frame per second). (a) Tomograms reconstructed using ITS software [26]. (b) Temperature distributions at time $t = 30$ min for the three fillings calculated from the normalized pixel permittivities using material-dependent cubic polynomial fit curves as exemplarily shown in section 4.3.2.

4.3.2. Calculation of pixel temperatures from ECT data for the FCDS-LQ3 catalyst. To convert the normalized pixel permittivities obtained from the ECT into temperatures, the curves from figure 6 were first approximated by third-order polynomials. The following polynomial was used for the FCDS-LQ3 catalyst, which led to a coefficient of determination $R^2 = 0.9999$ in the temperature range considered:

$$\varepsilon_{\mathrm{r,\,eff}}(\vartheta) = 1.816\mathrm{e}^{-7}\cdot\vartheta^3 - 2.384\mathrm{e}^{-5}\cdot\vartheta^2 + 9.230\cdot10^{-3}\cdot\vartheta + 4.981. \tag{12}$$

The relationship $\varepsilon_{r,\,\mathrm{eff}}(\vartheta)$ is then normalized to the temperature range between the temperatures of the calibration measurements of the ECT system. In the case at hand, the calibration was carried out with the FCDS-LQ3 catalyst at a temperature of $\vartheta_{\min} = 23°\mathrm{C}$ (room temperature) for the low reference permittivity and after uniform heating of the setup at $\vartheta_{\max} = 197°\mathrm{C}$ (measured with a thermocouple) for the high reference permittivity. The experiment was then continued as explained in section 4.2.

The normalized permittivity $\varepsilon_{r,\,\mathrm{norm}}(\vartheta)$ is calculated as follows from the effective permittivity of equation (12):

$$\varepsilon_{r,\,\mathrm{norm}}(\vartheta) = \frac{\varepsilon_{r,\,\mathrm{eff}}(\vartheta) - \varepsilon_{r,\,\mathrm{eff}}(\vartheta_{\min})}{\varepsilon_{r,\,\mathrm{eff}}(\vartheta_{\max}) - \varepsilon_{r,\,\mathrm{eff}}(\vartheta_{\min})}. \tag{13}$$

In order to convert the normalized pixel permittivities obtained from the ECT into temperatures in °C, the normalized characteristic curve from equation (13) is numerically inverted. This is done pixel by pixel for every normalized pixel permittivity using the Newton–Raphson method in the software Matlab [28], with the start value always set to

$$\vartheta_{\mathrm{start}} = \frac{\vartheta_{\max} - \vartheta_{\min}}{2}. \tag{14}$$

The following equation must therefore be solved for the temperature in the kth pixel ϑ_k using equation (13):

$$\frac{\varepsilon_{r,\,\mathrm{eff}}(\vartheta_k) - \varepsilon_{r,\,\mathrm{eff}}(\vartheta_{\min})}{\varepsilon_{r,\,\mathrm{eff}}(\vartheta_{\max}) - \varepsilon_{r,\,\mathrm{eff}}(\vartheta_{\min})} - g_k \overset{!}{=} 0, \tag{15}$$

where g_k is the normalized pixel permittivity in the kth pixel from the ECT image reconstruction, which replaces $\varepsilon_{r,\,\mathrm{norm}}(\vartheta)$ compared to equation (13).

Once all N pixels permittivities of a tomogram have been converted into temperatures, a radial temperature profile can be plotted on the basis of the calculated temperature values. For each of the radial temperature profiles shown in the following sections, the pixel temperatures were averaged annularly around the tube axis, see figure 10. For the comparison of the temperature measured with the thermocouple in the center of the fixed-bed, the calculated temperatures of the central four pixels were averaged.

4.3.3. Measurements with oxidized catalyst FCDS-LQ3. For reasons of simplicity for calibration of the ECT measuring system, the data points at room temperature ($\varepsilon_{r,\,\mathrm{low}} = 5.18$) and at 200 °C ($\varepsilon_{r,\,\mathrm{high}} = 7.31$) were taken from the corresponding curve from figure 6 to serve as reference permittivities, even though the real reference temperatures deviated slightly from these values, see section 4.3.2.

Figure 11(a) shows the experimental setup. The ECT-measured permittivities were converted into temperatures as explained in the previous section. For noise suppression, the pixel tempertures were first locally smoothed by time-averaging (moving time window over 20 frames) and then spatially smoothed by annular averaging over the eleven rings shown in figure 10. This led to the radial temperature profiles shown in figure 11(b), where the radii of the individual annuli correspond to the average radial positions of the centers of the pixels making up the respective annulus. The figure shows multiple temperature profiles at various times after the

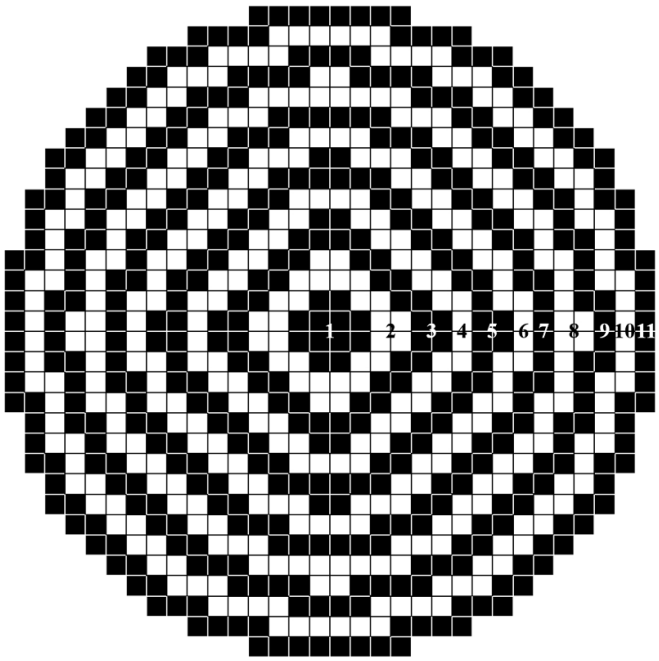

Figure 10. Discretization of the detection area (32 pixels across, 812 pixels in total). The 11 black or white rings visualize the pixel grouping used for annular averaging to obtain the radial temperature profiles.

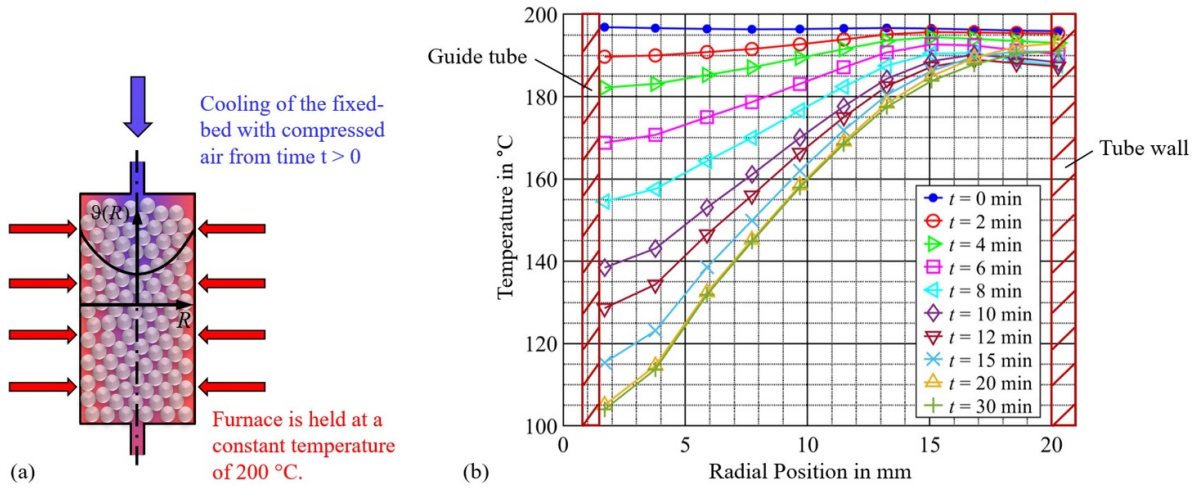

Figure 11. ECT-based observation of catalyst cooling. (a) Schematic view of the experiment. The previously hot fixed-bed reactor is cooled from the inside by injecting compressed air from $t = 0$. (b) Radial temperature profiles extracted from the ECT-measured permittivity distributions at various times.

cooling started. Looking at figure 11(b), the reconstructed temperature exhibits the expected behavior: only a small decrease with time at the tube wall, which is heated from the outside, and a large decrease with time near the tube axis, which is cooled by the air flow.

One aspect of the reconstructed solution, however, is counterintuitive at first: in the steady state, the radial temperature profile should have its largest slope near the wall due to the higher bulk porosity and therefore lower effective radial heat transfer coefficient of the tube filling [29]. This expected temperature profile has been plotted in figure 11(a). However, this only applies under the assumption that the hot fixed bed is subjected to a uniform flow velocity across the entire tube cross-section. In the tests carried out here, however, an abrupt change in cross-section occurs shortly before the air flow hits the hot fixed bed, which leads to a somewhat different temperature profile. After entering the fixed bed, a significantly higher flow velocity initially occurs in the tube axis than at the tube wall, which causes the largest temperature gradient in the upper part of the bed to occur in the center of the tube instead of at the wall. It can not be ruled out that this effect may still be present at the position of the measuring electrodes.

Even if the above effect does not apply, the deviation of the ECT-measured temperature profile from the undisturbed curve near the tube wall cannot be removed without more complex modeling strategies. Due to boundary effects the filling is

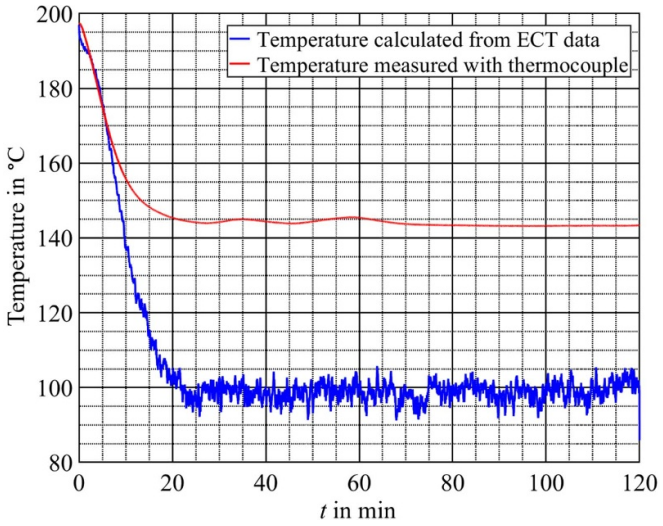

Figure 12. Comparison of the ECT-estimated fixed-bed core temperature with the temperature measured by the thermo-couple.

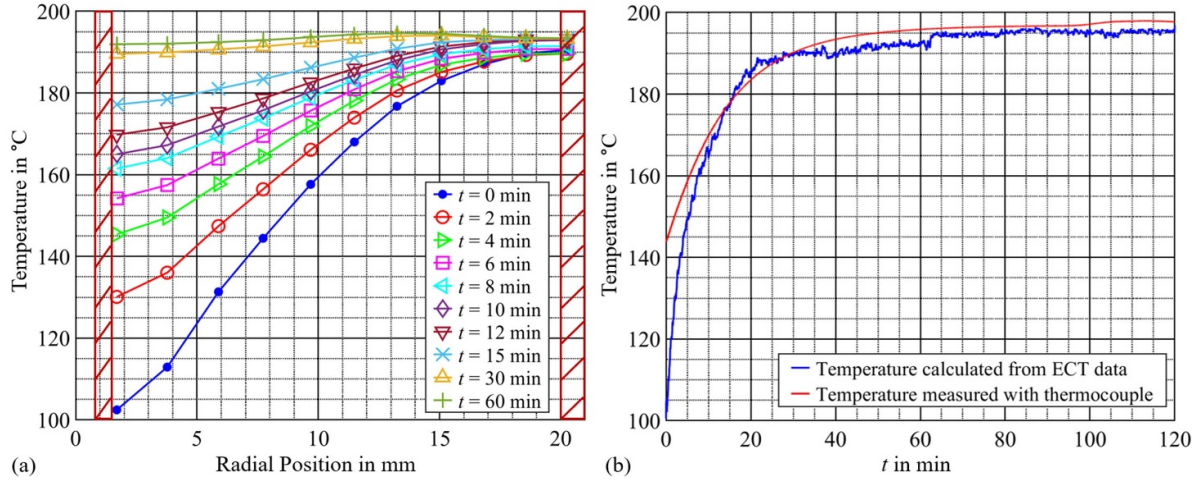

Figure 13. ECT-based observation of catalyst heating. The fixed-bed reactor was cooled by an air flow until the steady state was reached. At $t = 0$, the air flow was turned off. (a) Radial temperature profiles extracted from the ECT-measured permittivity distributions at various times. (b) Fixed-bed core temperature estimated by the ECT method and measured via thermocouple.

inhomogenious, more densely packed in the tube interior, less densely packed near the wall. This in turn means that different $\varepsilon_{r,\,\mathrm{eff}}(\vartheta)$ curves should be used for the inversion step, i.e. the inference of ϑ from the measured $\varepsilon_{r,\,\mathrm{eff}}$, near the tube axis and near the tube wall. In addition, the electrodes are attached to the outside of the tube wall, so that the temperature dependence of the wall material is inevitably measured and superimposed on the temperature effect of the filling material, as was shown in figure 9(a). No attempt has been made to include these effects in the model.

The steady-state on-axis, or core, temperature of the fixed-bed reactor determined by the ECT method deviates quite a bit from the temperature measured via the thermocouple placed in the guide tube along the tube axis (figure 12). As the time-dependence of the two temperature curves is very similar in shape, one is inclined to suspect a more systematic reason for the difference in the steady-state values. The most obvious model deficiency is the same as in the near-wall problem: the ceramic thermocouple guide tube present near the tube axis introduces a material inhomogeneity and would require the use of different $\varepsilon_{\mathrm{r,\,eff}}(\vartheta)$ curves for the inversion step near the axis and inside the catalyst bed. (Besides, note that the insertion of a thermocouple disturbs the catalyst bed and the gas flow. It is questionable if this yields the true temperature near the axis.) Again, no attempt has been made to take this effect into account. Without more complex models, the ECT-based temperature estimation must be considered most reliable within homogeneous material fillings and less so at media interfaces. Figure 13(a) shows the measurement results for a reheating experiment after the cooling air flow was turned off. Since the heat transfer takes place largely via heat conduction and heat radiation, it takes longer for the bed to reach its initial high temperature again than to cool down. As in figure 12, there exists a large deviation between the ECT-determined and the thermocouple-measured core temperature on the low-temperature side, which then disappears with increasing absolute temperature (figure 13(b)).

5. Summary and outlook

The results presented in this article show that the effective bulk permittivity of materials relevant to chemical engineering exhibits a temperature dependence that could be used to determine temperature profiles with ECT. Our experiments with ECT suggest that the method offers great potential as a non-invasive alternative to conventional temperature measurement techniques such as thermocouples inserted into reactors (and thus interfering with reactor operation). The results shown illustrate that ECT can detect temperature-dependent changes in effective bulk permittivity in situ. Relatively simple models yielded convincing quantitative values for the reconstructed temperature distributions inside homogeneous material fillings inside a fixed-bed reactor. No other method yields such distributions; thermocouples, for example, are restricted to local measurements and disturb their environment when they are inserted. But it became also evident that more complex models are needed for inhomogeneous material fillings, i.e. when the permittivity-vs.-temperature relationship becomes a function of the spatial coordinates. This is usually the case at media boundaries such as reactor tube walls or thermocouple guide tube walls.

Our tests have been limited to oxidized catalysts until now. Experiments under reaction conditions with reduced catalyst are the subject of future investigations.

Data availability statement

The data that support the findings of this study are available upon reasonable request from the authors.

Acknowledgments

The authors gratefully acknowledge the financial support of the Bavarian State Ministry of Education, Science and the Arts within the framework Gradiertenkolleg Energieautarke Gebäude of the TechnologieAllianz Oberfranken (TAO).

Conflict of interest

The authors declare no conflicts of interest.

ORCID iDs

Michael Weiss https://orcid.org/0009-0009-6104-4027
Alice Fischerauer https://orcid.org/0009-0000-4477-3361
Andreas Jess https://orcid.org/0000-0001-6038-7866
Gerhard Fischerauer https://orcid.org/0000-0003-2000-4730

References

[1] Shen J, Li Y, Ho W H, Liu X and Hildebrandt D 2021 Experimental and simulation study of the temperature distribution in a bench-scale fixed bed *AIChE J.* **67** 1–14
[2] Zenner A, Fiaty K, Bellière-Baca V, Rocha C, Gauthier G and Edouard D 2019 Effective heat transfers in packed bed: experimental and model investigation *Chem. Eng. Sci.* **9** 424–36
[3] Andrigo P, Bagatin R and Pagani G 1999 Fixed bed reactors *Catal. Today* **52** 197–221
[4] Stegehake C, Grünewald M, Zanthoff H and Hecht C 2018 Fiber-optic temperature measurements in fixed-bed reactors for model-based evaluation of effective radial thermal conductivity *Chem. Ing. Tech.* **5** 602–14
[5] Ulpts J, Dreher W, Klink M and Thöming J 2015 NMR imaging of gas phase hydrogenation in a packed bed flow reactor *Appl. Catal.* A **502** 340–9
[6] Stegehake C and Grünewald M 2017 Anwendung von faseroptischer Messechnik zur gering-invasiven Temperaturprofilmessung in Reaktoren *Chem. Ing. Tech.* **89** 480–5
[7] Gamio J C, Castro J, Rivera L, Alamilla J, Garcia-Nocetti F and Aguilar L 2005 Visualisation of gas–oil two-phase flows in pressurised pipes using electrical capacitance tomography *Flow Meas. Instrum.* **16** 129–34
[8] Huang K, Meng S, Guo Q, Ye M, Shen J, Zhang T, Yang W and Liu Z 2018 High-temperature electrical capacitance tomography for gas–solid fluidised beds *Meas. Sci. Technol.* **10** 104002
[9] Ho Yang S, Sik Kim Y, Dagalakis N G and Wang Y 2021 Flexible assemblies of electrocapacitive volume tomographic sensors for gauging fuel of spacecraft *J. Spacecr. Rockets* **58** 499–504
[10] Liu J, Liu S, Liu Y, Schlaberg H I and Lei J 2015 Study of flame characteristics using electric capacitance tomography *Energy Proc.* **12** 229–32
[11] Wondrak T and Soleimani M 2017 A novel metal flow imaging using electrical capacitance tomography *Meas. Sci. Technol.* **6** 064001
[12] Hu D, Tian Y, Chang L, Sun S, Sun J, Cao Z and Xu L 2020 Estimation of combustion temperature field from the electrical admittivity distribution obtained by electrical tomography *IEEE Trans. Instrum. Meas.* **69** 6271–80
[13] Dyakowski T, York T, Mikos M, Vlaev D, Mann R, Follows G, Boxman A and Wilson M 2000 Imaging nylon polymerisation processes by applying electrical tomography *Chem. Eng. J.* **77** 105–9
[14] Chen Q and Liu S 2012 Flame imaging in meso-scale porous media burner using electrical capacitance tomography *Chin. J. Chem. Eng.* **20** 329–36
[15] Liu J, Liu S, Zhou W, Kang Y and Schlaberg H I 2017 Flame detection on swirl burner using ECT with dynamic reconstruction algorithm based on the split bregman iteration *IEEE Sens. J.* **17** 7290–7
[16] Hirose Y, Sapkota A, Sugawara M and Takei M 2016 Noninvasive real-time 2D imaging of temperature distribution during the plastic pellet cooling process by using electrical capacitance tomography *Meas. Sci. Technol.* **1** 015403
[17] Yang Y, Yang W and Zhong H 2008 Temperature distribution measurement and control of extrusion process by tomography *2008 IEEE I. W. Imag. Syst. Techni.* (*Chania, Crete, Greece*, *10–12 September 2008*) pp 170–4
[18] Yang W Q and Peng L 2003 Image reconstruction algorithms for electrical capacitance tomography *Meas. Sci. Technol.* **14** R1–R13
[19] Kotre C J 1994 EIT image reconstruction using sensitivity weighted filtered backprojection *Physiol. Meas.* **15** A125–36
[20] Wang M 2002 Inverse solutions for electrical impedance tomography based on conjugate gradients methods *Meas. Sci. Technol.* **13** 101–17

[21] Penrose R 1956 On best approximate solutions of linear matrix equations *Math. Proc. Camb. Phil. Soc.* **52** 17–19
[22] Weiss M, Fischerauer G and Jess A 2023 E5.3—suitability of ECT for non-invasive temperature monitoring in fixed-bed reactors *Proc. SMSI 2023 Conf.: Sensor and Measurement Science Int.* (*Nuremberg, Germany*) pp 259–60
[23] Keysight Technologies 2022 Datasheet for E4990A impedance analyzer (available at: www.keysight.com/us/en/assets/7018-04256/data-sheets/5991-3890.pdf)
[24] National Instruments 2023 What is LabVIEW? graphical programming for test & measurement—NI (available at: www.ni.com/en/shop/labview.html)
[25] Tauer G S 2021 Verhalten eines wandgekühlten Festbettreaktors zur CO_2-Methanisierung bei instationären Betriebsbedingungen *Dissertation* Department of Chemical Engineering, University (available at: https://epub.uni-bayreuth.de/id/eprint/5881/1/Dissertation_Final_Tauer.pdf)
[26] Industrial Tomography Systems Ltd 2023 M3c—electrical capacitance tomography—products—ITS (available at: www.itoms.com/products/m3c-electrical-capacitance-tomography/)
[27] Ho J and Jow R 2009 *Characterization of High Temperature Polymer Thin Films for Power Conditioning Capacitors* (U.S. Army Research Laboratory)
[28] The MathWorks, Inc. 2024 MATLAB (available at: www.mathworks.com/products/matlab.html)
[29] Jess A and Wasserscheid P 2020 *Chemical Technology. From Principles to Products* 2nd edn (Wiley)